Contents lists available at ScienceDirect

Heliyon

Research article

Estimation of optimized timely system matrix with improved image quality in iterative reconstruction algorithm: A simulation study

Vahid Moslemi [a], Vahid Erfanian [b], Mansour Ashoor [a,*]

[a] Radiation Applications Research School, Nuclear Science and Technology Research Institute, P.O. Box: 113653486, Tehran, Iran
[b] Mechanical Engineering Department, Amirkabir University of Technology, P.O. Box: 158754413, Tehran, Iran

ARTICLE INFO

ABSTRACT

The system matrix (SM) being a main part of statistical image reconstruction algorithms establishes relationship between the object and projection space. The aim was to determine it in a short duration time, towards obtaining the best quality of contrast images. In this study, a new analytical method based on Cavalieri's principle as subdividing common regions has been proposed in which the precision of the amounts of estimated areas was improved by increasing the number of divisions (NOD), and consequently the total SM's time was increased. An important issue is the tradeoff between the NODs and computational time. For this purpose, a Monte Carlo simulated Jaszczak phantom study was performed by the Monte Carlo N-Particle transport code version 5 (MCNP5) in which the tomographic images of resolution and contrast phantoms were reconstructed by maximum likelihood expectation maximization (MLEM) algorithm, and the influence of NODs variations was investigated. The results show that the lowest and best quality have been obtained at the NODs of 0 and 8, respectively and in the optimum case, the SM's total time at NOD of 8 was 925 s, which was much lower than those of the conventional Monte Carlo simulations and experimental test.

1. Introduction

Image reconstruction algorithms play a key role to obtain the anatomical and functional maps towards better recognition in the medical fields. The shorter the time of algorithm, the better temporal resolution of images will be. This is an important aim in nuclear medical imaging because making internal functionality of the organs more apparent, and projections are converted to transaxial images by these algorithms, which are categorized in analytical and iterative methods [1, 2, 3, 4, 5, 6, 7, 8, 9, 10, 11]. The maximum likelihood expectation maximization (MLEM) algorithm is used to reconstruct tomographic images by iteratively maximizing a likelihood function. The slow convergence rate and high computational cost are major shortcomings of the MLEM [12, 13]. The thresholding technique is a solution to speed up the convergence rate of MLEM algorithms [14, 15, 16].

The system matrix (SM) indicating relationship between the object and projection space is a main part of statistical image reconstruction algorithms. It is calculated by three methods as; (i) analytical method in which the common regions (CR) considering as interacting probability of emitted gamma photons with detector

elements are calculated by geometrical relations [17, 18, 19, 20, 21]; (ii) Monte Carlo (MC) simulations by modeling a digital phantom and estimating projections, which the ratio of counts in i-th element of detector for the originated photons from j-th pixel of object matrix is considered as $a_{i,j}$ element of the SM [22, 23, 24]; and (iii) experimental method where the SM is obtained by measuring projections around the phantoms [25, 26].

In this study, a new analytical method based on Cavalieri's principle namely as subdividing common regions (SCR) algorithm have been proposed to estimate the optimized timely SM. In the proposed method, due to intersection between detector element path and pixel border, the common region (CR) was divided into even-smaller parts and the total CR area was calculated using trapezoidal integration rule. Finally, the influence of number of divisions (NOD) on the precision of the amount of CR area and the quality of tomographic images using a Monte Carlo simulated Jaszczak phantom by the Monte Carlo N-Particle version 5 (MCNP5) code was investigated and an optimum NOD was introduced.

---

2. Materials and methods

2.1. Theory

The SM has been calculated by the probability of recording emitted gamma photons from a voxel of object by a detector element at a distinct detector angle towards the generation of projections. In other words, the interacting probability of the photons from the *ij*-pixel of object matrix with *k*-element of detector depends on the position of the element related to the corresponding pixel. In emission computed tomography, the correlation between the photons from the object matrix (f) and generated projection on the detector plane (g) is as follows:

$$g = A \times f. \tag{1}$$

where A is the SM. An 4×4 object matrix and a 4-element detector array are shown in Figure 1. The CR between pixel borders and detector element virtual paths have been made by covering the detector element (g2) upon F6 pixel, indicating as $a_{2,6}$ of the SM. The CRs go on values between 0 and 1. In other words, while the path of *k*-th detector element does not interact with *ij*-th image pixel, then the probability of interacting is 0. In contrast, while the detector element completely covers the pixel, it will be 1. For the situations that the detector element covers a portion of pixel area, it has the values between 0 and 1. The precision on the amount of CR has a direct effect on the quality of the reconstructed images in MLEM.

Eq. (1) may be rewritten for one projection at a distinct detector angle in Figure 1 as follows:

The CRs based on the Cavalieri's principle were divided as smaller parts, and the entire area of CR was determined through summation of the area of these parts by trapezoidal integration rule. Figure 2 exhibits the implementation of SCR method to calculate the CR on the pixel.

Passing the hypothetical path of detector element (g) through pixel border creates a polygonal CR as $\mathbf{a}'\mathbf{b}'\mathbf{c}'\mathbf{abc}$. In the first step, the linear segments of aa' and cc' were placed beside each other with the distance of g to estimate the area. The polygonal of $\mathbf{aca'c'}$ in Figure 3(a) has a lower area in compared to that of the desired CR. In the second step, a line from the middle of CR causes to divide into two new equivalent parts to have a better estimation. By placing linear segments of aa' and oo' with the distance of the $\frac{g}{2}$, and similarly oo' and cc' with distance of the $\frac{g}{2}$ a new polygonal of $\mathbf{aoc\,a'o'c'}$ was made, which its area determined by trapezoidal integration is closer to the desired CR, as shown in Figure 3(b). In the third step, the CR was divided into four parts and new polygon was constructed by five linear segments, as shown in Figure 3(c). The distance between aa' and next line segment is the $\frac{g}{4}$. The area of obtained polygonal in this step equals to that of the desired CR in Figure 2. Thus, the estimated area approaches to the desired value in four divisions. However, the area of CR was estimated here correctly by four divisions, but for other situations more divisions might be required. The precision of estimations was improved by increasing divisions.

The length of passing line segments through the CR are changed by the variation of the detector angle. By defining the centre of image matrix as the origin of a polar coordinate system at detector angle of zero ($\theta = 0°$), the passing lines from the detector with k elements through the image pixels can be characterized as:

$$\begin{bmatrix} g1 \\ g2 \\ g3 \\ g4 \end{bmatrix} = \begin{bmatrix} a_{1,1} & a_{1,2} & a_{1,3} & a_{1,4} & a_{1,5} & a_{1,6} & 0 & 0 & 0 & 0 & 0 & 0 & 0 & 0 & 0 & 0 \\ 0 & a_{2,2} & a_{2,3} & a_{2,4} & a_{2,5} & a_{2,6} & a_{2,7} & a_{2,8} & a_{2,9} & a_{2,10} & 0 & 0 & 0 & 0 & 0 & 0 \\ 0 & 0 & 0 & 0 & 0 & 0 & a_{3,7} & a_{3,8} & a_{3,9} & a_{3,10} & a_{3,11} & a_{3,12} & a_{3,13} & a_{3,14} & a_{3,15} & 0 \\ 0 & 0 & 0 & 0 & 0 & 0 & 0 & 0 & 0 & 0 & a_{4,11} & a_{4,12} & a_{4,13} & a_{4,14} & a_{4,15} & a_{4,16} \end{bmatrix} \times \begin{bmatrix} f1 \\ f2 \\ f3 \\ \bullet \\ \bullet \\ \bullet \\ f14 \\ f15 \\ f16 \end{bmatrix} \tag{2}$$
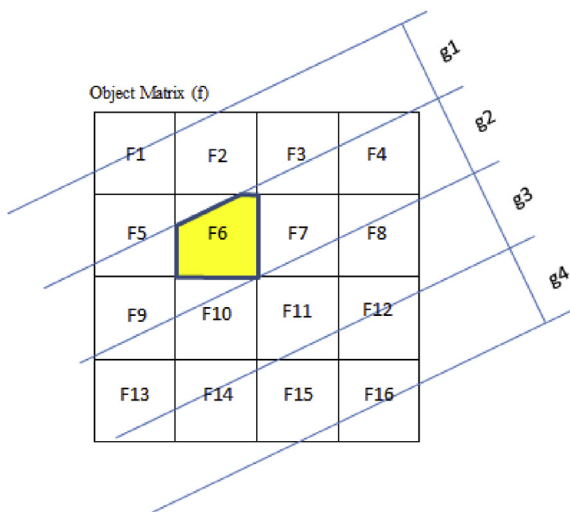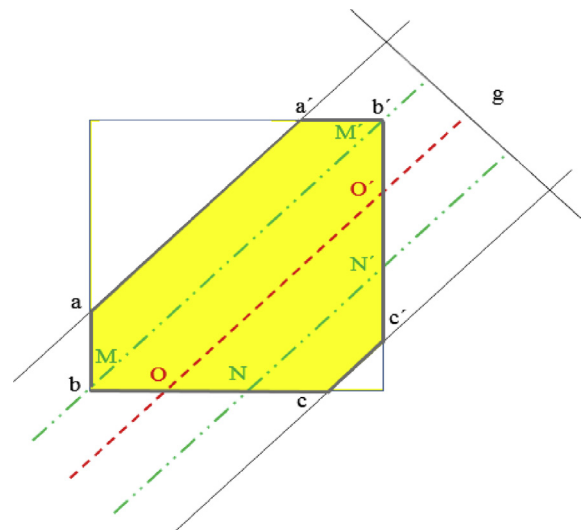

Figure 1. Covering the image matrix (F6) by the detector element (g2), as yellow cross section area.

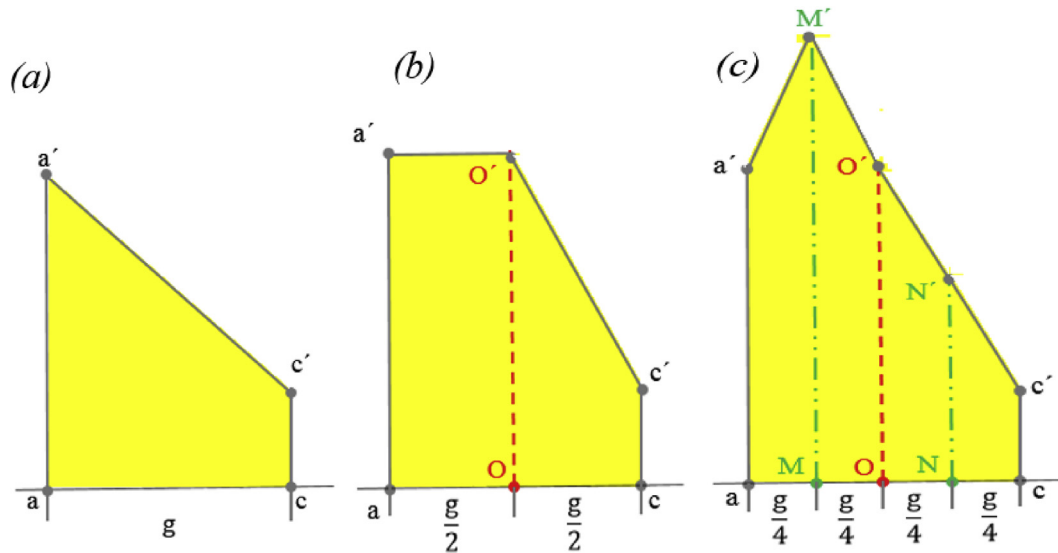**Figure 2.** Implementation of the SCR to calculate the area of CR on the pixel.

Figure 3. The illustration of modeling CR (a) without SCR method, (b) twofold and (c) fourfold subdivision, using Cavalieri's principle.

$$y = g_k \tag{3}$$

where the g_k equals to the width from the origin. By increasing the detector angle on the range from 0 to 45°, the passing lines through image may be formulated as follows:

$$y = (\tan\theta)x + \frac{1}{\cos\theta}g_k \tag{4}$$

Assuming the $F_{i,j}$ as unitary pixel in an $n \times n$ image matrix, as shown in Figure 4, the passing (red) lines through the pixel have three situations that one may obtain; (a) the length of (**1**) segment placed in the up-left side of pixel (Δl) as:

$$\Delta l = \left[\frac{1}{\tan\theta}\left(\frac{n}{2} - i - \frac{g_k}{\cos\theta} + 1\right) - \left(j - \frac{n}{2} - 1\right) \right] \frac{1}{\cos\theta} \tag{5}$$

(b) the length of (**2**) segment in the left-right side of pixel as:

$$\Delta l = \frac{1}{\cos\theta} \tag{6}$$

and, (c) the length of (**3**) segment in the right-down side of pixel as:

$$\Delta l = \left[\left(j - \frac{n}{2}\right) - \frac{1}{\tan\theta}\left(\frac{n}{2} - i - \frac{g_k}{\cos\theta}\right) \right] \frac{1}{\cos\theta} \tag{7}$$

In general, the passing line segments through pixel sides are categorized in one of the above mentioned scenarios and there is no other situation.

The geometric symmetry principle was used to calculate the length of line segments in the other degrees. By mirroring procedure, all data from 45° to 90° were obtained using the angles from 0° to 45° related to the axis of $45°$. This procedure was continued and all data of the SM in $360°$ was calculated to reduce the computational time. Our analytical algorithm was implemented for $1/8$ of the SM and the rest of the SM data were completed by repeating and mirroring technique.

By increasing the NODs in a detector element, the precision of estimated CR area is increased due to intersection between pixel areas and detector element in a distinct angle, and as the NODs approaches infinity, the difference between the estimated and desired areas goes to zero. Since increasing the NODs increases the computational time, thus the
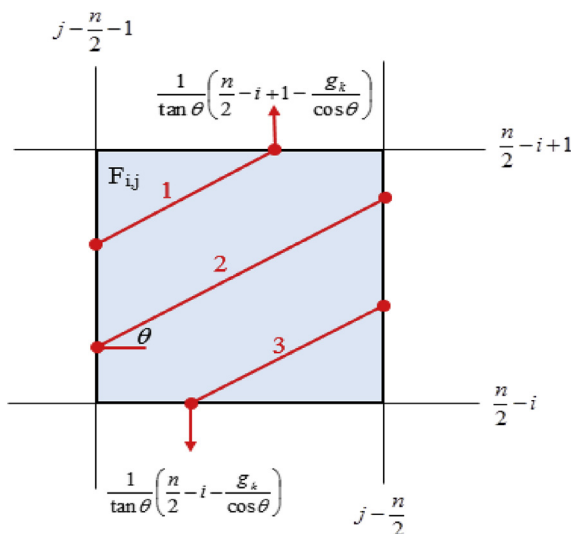

Figure 4. Passage of line segments through a pixel (three red situations, 1-2-3).
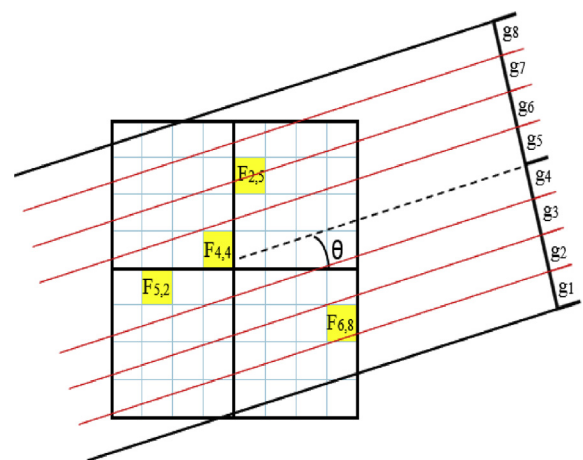

Figure 5. Intersection between the detector elements and the pixels of $F_{2,5}$, $F_{4,4}$, $F_{5,2}$ and $F_{6,8}$ in the object matrix to evaluate the precision of the estimated area for different NODs.
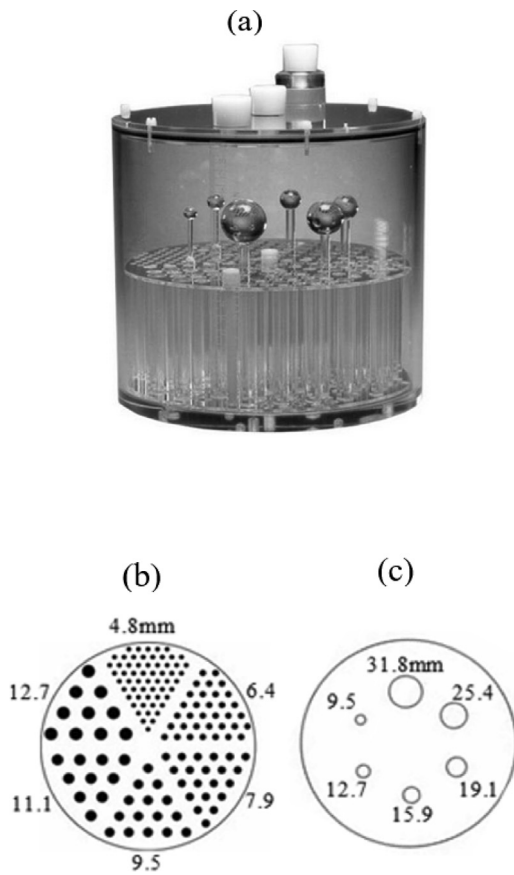
Figure 6. (a) Jaszczak phantom (ECT/DLX/p); (b) spatial resolution; and (c) contrast of images.

optimization of NOD was necessary to minimize the duration of the SM calculation time.

To evaluate the precision of estimated CR area for different NODs, the pixels of $F_{2,5}$, $F_{4,4}$, $F_{5,2}$ and $F_{6,8}$ in the size of 8×8 were selected, as shown in Figure 5. The 8-element detector was placed at angles of 2°, 99°, 192° and 285° related to center of image matrix and the CR area was calculated using SCR method. This area was estimated without any divisions in the first step, but for the next steps the detector elements were subdivided into even similar parts incrementally. In each detector angle, the selected pixels were matched with different detector elements, and the CR area was estimated for different divisions.

2.2. Monte Carlo simulation-spatial resolution and contrast using Jaszczak phantom

The Jaszczak phantoms are used in nuclear medicine imaging studies to evaluate spatial resolution and contrast of tomographic images. The Jaszczak phantom model (ECT/DLX/p) was selected to investigate the effects of NODs on the quality of images, as shown in Figure 6(a). The MC simulations were performed by the MCNP5 code [27]. The phantom was divided into two parts including spatial resolution and contrast of images. The first part was a bar phantom to evaluate spatial resolution in tomographic images and contains of 6 cylindrical bar groups with diameters of 4.8, 6.4, 7.9, 9.5, 11.1 and 12.7 mm, as shown in Figure 6(b). In the simulations, these bars were filled with a homogenous 140-keV radioactive Technetium solution with the 100-MBq/cc activity concentrations and the volume around the bars was filled by water. The second part was contrast phantom and contained 6 spheres with diameters of 9.5, 12.7, 15.9, 19.1, 25.4 and 31.8 mm, as shown in Figure 6(c). The spheres with diameters of 9.5, 12.7, 15.9 and 19.1 mm were filled by a homogenous radioactive Technetium (Tc-99m) solution with the energy

and activity concentration of 140-keV and 800-MBq/cc respectively as hot lesions, and the 25.4 and 31.8-mm spheres without any activity concentrations were modeled as cold lesions. Since the activity concentrations of surrounding volume the spheres were 100 MBq/cc, the real contrast for hot and cold spheres to background became 8/1 and 0/1, respectively.

In addition, an standard LEHR lead collimator with hexagonal hole size, hole length and septa thickness of 1.5, 35 and 0.25mm, respectively was modeled and simulated. The NaI detector was divided into separate rows with 128 cubic cells and dimensions of $1.75 \times 1.75 \times 9.525$ mm to calculate the simulated projections.

To reconstruct the tomographic images of phantom, the 120 projections were obtained in a 360° rotation around the phantom in 3°-steps. The distance of collimator to the center of phantom and distance between collimator to detector were 150 and 5 mm, respectively. To calculate each projection, 2×10^{10} photons were run and signal intensity in detector cells were calculated by F8 tally in which the interacting photons in a cell is considered as pulse height distribution. The statistical error of simulations was fewer than 5%.

2.3. MLEM image reconstruction algorithm and image analysis

Expectation maximization algorithm is an approach to iterative computation of maximum likelihood estimates when the observations can be viewed as incomplete data. In this study, the MLEM algorithm was developed by the MATLAB software to reconstruct tomographic images of resolution and contrast phantoms in which its process is given as follows [28]:

$$\overline{f}_j^{(k+1)} = \frac{\overline{f}_j^{(k)}}{\sum_{i=1}^{n} a_{ij}} \sum_{i=1}^{n} \frac{g_i}{\sum_{j'=1}^{m} a_{ij'} \cdot \overline{f}_{j'}^{(k)}} a_{ij} \qquad (8)$$

where $\overline{f}_j^{(k+1)}$, $\overline{f}_j^{(0)}$, g_i and a_{ij} are the latest estimated image from *k*-th iteration, the first estimation as a uniform disc, the projection value in the *i-th* element of detector and the SM, respectively. The data of projections (g) was arranged in a 128×128 matrix and the SMs were calculated for various NODs of 2, 4, 8, 16, 32 and 1024. Tomographic images of resolution and contrast phantoms were reconstructed for 100 iterations in the MLEM.

To assess the tomographic image quality of contrast phantom, the contrast recovery coefficient (CRC%) may be defined as follows [29]:

$$CRC\% = \frac{\frac{\mu_I - \mu_b}{\mu_b}}{C - 1} \times 100 \qquad (9)$$

Over the lesions (hot and cold) and background as shown in Figure 9(e), the average intensity on each pixel was calculated as μ_I and μ_b respectively. C is the real contrast, which was 8 and 0 for hot and cold lesions, respectively. The noise coefficient (NC%) in images was evaluated by calculating standard deviation of pixel values in ROI at the central region of contrast image (σ_b) as follows [29]:

$$NC\% = \frac{\sigma_b}{\mu_b} \times 100 \qquad (10)$$

The contrast to noise ratio (CNR) as a criterion for evaluating image quality was calculated for all lesions as follows [29]:

$$CNR = \frac{CRC}{N_C} \qquad (11)$$

3. Results and discussion

Figure 7 shows the values of estimated CR area of $F_{2,5}$, $F_{4,4}$, $F_{5,2}$ and $F_{6,8}$ pixels at detector angles of 2°, 99°, 192° and 285° at various NODs. It is found that these values depend on the detector position at various
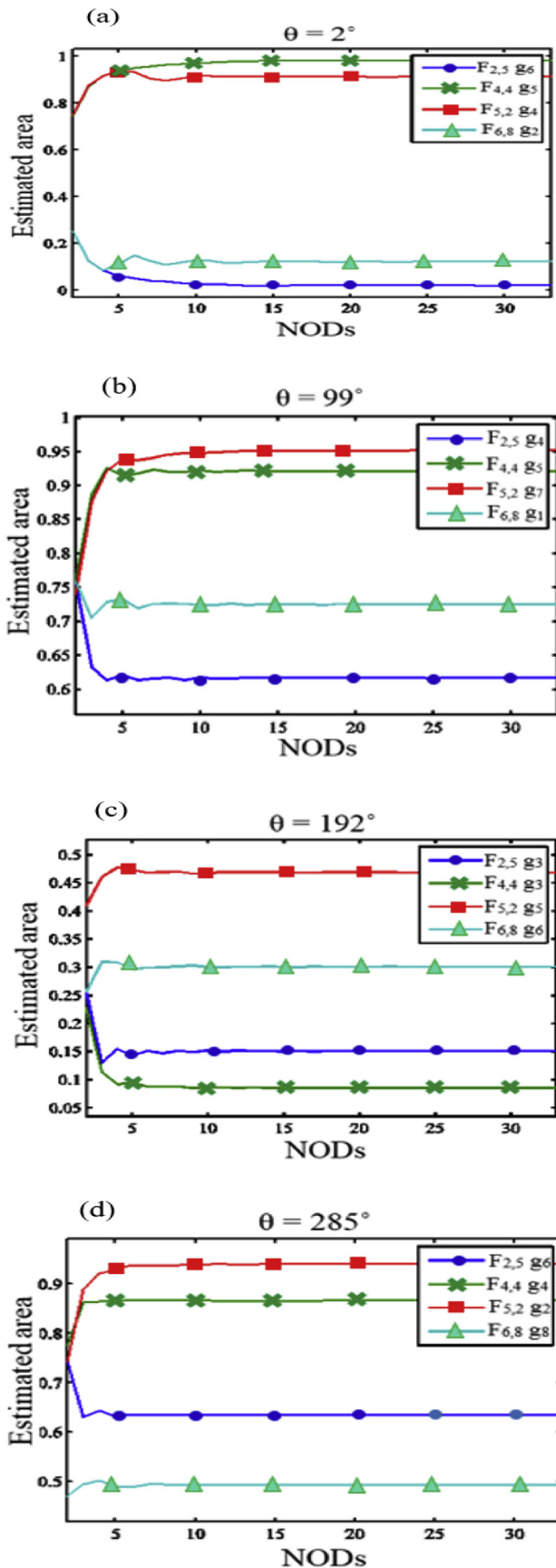
Figure 7. Estimated area of the CR in pixels of $F_{2,5}$, $F_{4,4}$, $F_{5,2}$ and $F_{6,8}$ for different NODs at detector angles of (a) 2°, (b) 99°, (c) 192° and (d) 285°.
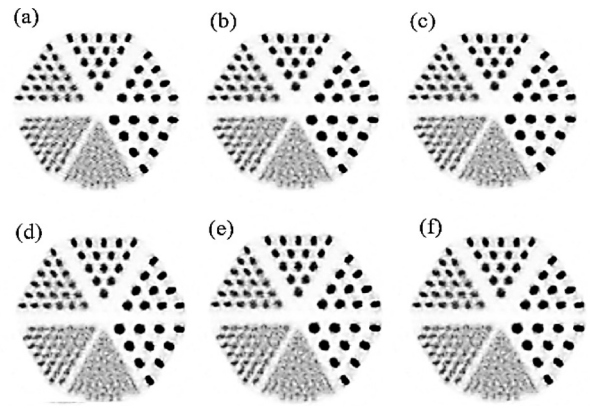

Figure 8. Reconstructed tomographic images of spatial resolution phantom for NODs of (a) 0, (b) 2, (c) 4, (d) 8, (e) 16 and (f) 1024.
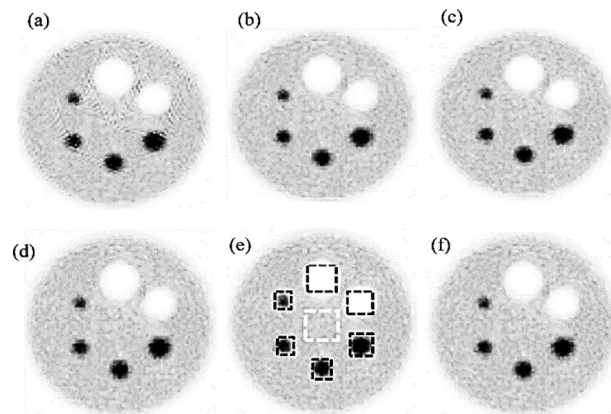

Figure 9. Reconstructed images of contrast phantom for NODs of (a) 0, (b) 2, (c) 4, (d) 8, (e) 16 and (f) 1024. Mean pixel intensity values for hot and cold lesions and for the background in black and white dashed squares on the images, respectively were calculated.

angles with respect to the CR changes in Figure 7. For instance, the pixel of $F_{5,2}$ at detector angles of 2°, 99°, 192° and 285° was intersected with detector elements of g_4, g_5, g_7 and g_2, respectively. Estimated areas in low divisions had intense fluctuations. They converged to their desired values by increasing divisions. For the NODs less than 10, the estimated areas in four pixels were changed for different divisions. The estimated areas tend to their desired values by increasing NOD more than 10, and the curves became smoother. In other words, the fluctuations were almost removed, and the difference with desired values tend to become zero.

The reconstructed tomographic images of resolution phantom for the SMs with the NODs of 0, 2, 4, 8, 16 and 1024 had the same quality and the number of division did not affect the quality of images, as shown in Figure 8.

Figure 9 exhibits the tomographic images of contrast phantom obtained for the SMs with the NODs of 0, 2, 4, 8, 16 and 1024. The quality of tomographic images for different NODs was assessed quantitatively through the contrast phantom images. The maximum image distortion was observed in contrast image obtained for NOD of 0, as shown in Figure 9(a). Additionally, the maximum noise and the minimum CNR was found in this image. Since the CNR is a criterion to evaluate the quality of images, the obtained image for 0 divisions had the lowest quality.

The NC% was determined by calculating the average and standard deviation of pixel values of ROI (white dashed square in Figure 9(e)) over the central part of contrast phantom images. Figure 10 shows the changes of NC% for NODs of 0, 2, 4, 8, 16 and 1024. Variations of NC% indicates
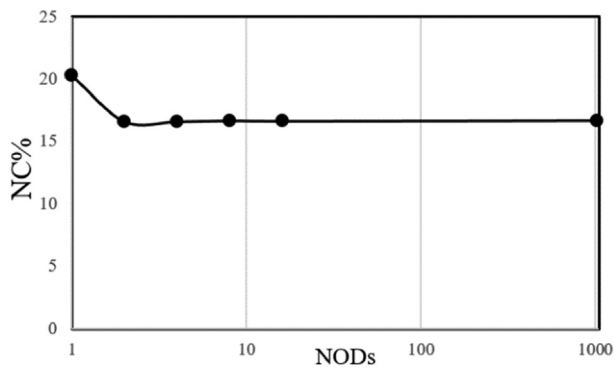
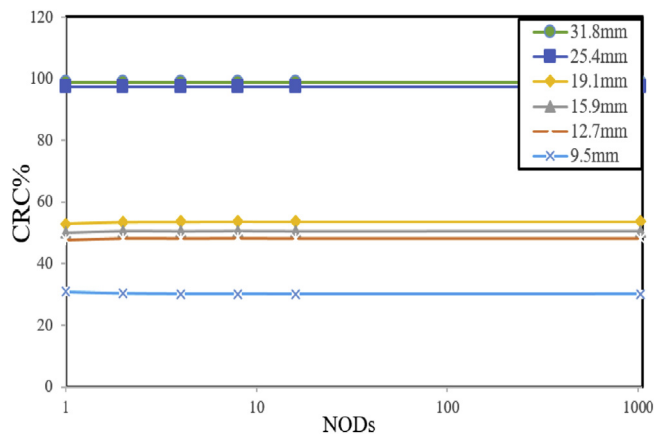**Figure 10.** The NC% values of hot and cold spheres at various NODs.

Figure 11. The CRC% values of hot and cold spheres at various NODs.
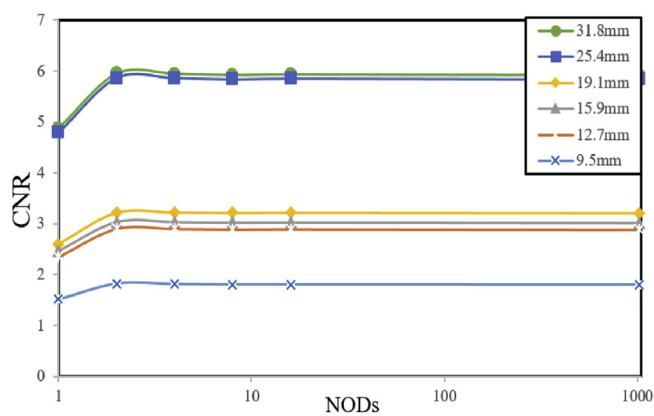

Figure 12. The CNR values of hot and cold spheres at various NODs.

that more noise in images was found at the NOD of 0, while by increasing NODs the noise was reduced, and the noise values in the images are the same for NODs more than the 8 value.

The contrast recovery coefficient of all lesions for various NODs were acquired by calculating the average of pixel values in ROI over the hot and cold lesions (black dashed squares). Figure 11 shows the changes of

CRC% of hot lesions with diameters of 9.5, 12.7, 15.9 and 19.1mm and cold lesions with diameters of 25.4 and 31.8 mm for different NODs. The CRC% values are independent from the number of NODs, although low changes may be seen in hot lesions at the NOD of 0.

The CNR values of hot and cold lesions for different NODs are shown in Figure 12. The quality of tomographic images at the NOD of 0 has the lowest quality, but it is improved by increasing the NODs, and the quality of images for NODs more than the 8 value is the same. Regard to the NC and CNR values, it was found that by increasing NODs from 0 to 2 the quality of contrast images were significantly improved. Furthermore, the images indicate similar quality for more than the 8 divisions. Also, the images with 8 and 1024 divisions had the same quality.

One of the most important problems associated at calculating the SM is the required time for obtaining all arrays. A personal computer with 4 cores of 2.5 GHz Intel CPUs was used for calculation of times of the SMs at the NODs of 0, 2, 4, 8, 32 and 1024, as shown in Table 1. In our analytical algorithm, the total time for 1024 divisions was around 17 h in compared to the required time for producing the SM by MC simulations that might take more than 70 days [30]. The generation of the SM in a short time is the main advantage of our method relative to the other ones. An important issue in the generation of the SM is the tradeoff between NODs or precision of calculations and the computational time. These times summarized in Table 1 indicate that by increasing NODs, the calculation time is increased incrementally. Therefore, it is necessary to find an optimum number for divisions to improve this trade off. Optimizing the NOD results in achieving images with appropriate quality with minimum computational time and acceptable precision. With respect to the precision of estimated CR areas and the quality of produced images for different divisions, producing the SM with NOD of 8 and the total time of 925 s was selected as the optimum case.

The real applications of this method in the medical world are while the images have been acquired from the single photon emission computed tomography (SPECT) system as well as the positron emission tomography (PET) and computed tomography (CT) ones in which the implementation of the iterative reconstruction algorithm is time-consuming due to the computing system matrix being a very important part in obtaining reconstructed images should be done. In general, the SM needs to be recomputed while there are any geometrical changes of detection systems in medical devices. In this study, the theoretical concepts of computational algorithms were first explained and then SM was calculated and by using of calculated projections of Jaszczak phantom obtained by MCNP simulations, transaxial images for different NODs were reconstructed. The presented algorithm is able to improve the time limitation of the iterative algorithm as well as may be used for image reconstruction of industrial CT scans. Despite of medical CT scans which usually have the same geometrical specifications, the industrial CTs are constructed with various geometrical specifications because the industrial facilities need to use CTs with different dimensions along with different detector sizes and types [31, 32]. The presented method may help designers, who have to survey and investigate the effects of different geometrical specifications on the quality of the images and achieve the optimized design in a short time. The method may be also implemented for small animal SPECT imaging where the images are acquired by different multipinhole collimators [33]. Its corresponding system matrix for each collimator type may be computed and the images are reconstructed exclusively in a short time.

4. Conclusion

In this study, a novel analytical method was proposed to estimate the SM in a short duration time based on Cavalieri's principle towards the best quality of images. By increasing the number of divisions, the precision of estimated CR area was improved, and consequently the total SM's time was increased. The results show that the lowest and best quality have been obtained at the NODs of 0 and 8, respectively and in the optimum case, the SM's total time at NOD of 8 was 925 s, which was

Table 1. Computational times at various NODs. The SM with the NOD of 8 and total computational time of 925 s was selected as the optimum case.

NOD	0	2	4	8	32	1024
calculation time (sec)	575	604	684	**925**	4534	62028

much lower than those of the conventional Monte Carlo simulations and experimental test. Thus, the proposed method can expedite the deploying iterative reconstruction in clinical uses along with the best image quality.

Declarations

Author contribution statement

Mansour Ashoor: Conceived and designed the experiments; Analyzed and interpreted the data; Contributed reagents, materials, analysis tools or data; Wrote the paper.

Vahid Moslemi: Conceived and designed the experiments; Performed the experiments; Analyzed and interpreted the data.

Vahid Erfanian: Performed the experiments; Analyzed and interpreted the data.

Funding statement

Competing interest statement

The authors declare no conflict of interest.

Additional information

No additional information is available for this paper.

References

[1] B.C. Tai, et al., Delimitated strike artifacts from FBP using a robust morphological structure operation, Radiat. Phys. Chem. 97 (April 2014) 31–37.

[2] N.E. Protonotarios, G.M. Spyrou, A. Kastis, Automatic cumulative sums contour detection of FBP-reconstructed multi-object nuclear medicine images, Comput. Biol. Med. 85 (June 2017) 43–52.

[3] R.A. Brooks, G. Di Chiro, Principles of computer assisted tomography (CAT) in radiographic and radioisotopic imaging, Phys. Med. Biol. 21 (1976) 689–732.

[4] D.B. Kay, J.W. Keyes, W. Simon, Radionuclide tomographic image reconstruction using Fourier transform techniques, J. Nucl. Med. 15 (1974) 981–986.

[5] A.C. Kakand, M. Slaney, Principles of Computerized Tomographic Imaging, 49–112, IEEE Press, New York, NY, USA, 1988.

[6] P.R. Edholm, G.T. Herman, Linograms in image reconstruction from projections, IEEE Trans. Med. Imaging 6 (1987) 301–307.

[7] P.R. Edholm, G.T. Herman, D.A. Roberts, Image reconstruction from linograms: implementation and evaluation, IEEE Trans. Med. Imaging 7 (1988) 239–246.

[8] T. Bortfeld, U. Oelfke, Fast and exact 2D image reconstruction by means of Chebyshev decomposition and backprojection, Phys. Med. Biol. 44 (1999) 1105–1120.

[9] B.I. Andia, K.D. Sauer, C.A. Bouman, Nonlinear backprojection for tomographic reconstruction, IEEE Trans. Nucl. Sci. 49 (2002) 61–68.

[10] V. Moslemi, M. Ashoor, Introducing a novel parallel hole collimator: the theoretical and Monte Carlo investigations, IEEE Trans. Nucl. Sci. 64 (9) (2017) 2578–2587.

[11] P.P. Bruyant, Analytic and iterative reconstruction algorithms in SPECT, J. Nucl. Med. 43 (10) (Oct. 2002) 1343–1358.

[12] A.J. Rockmore, A. Mackovski, A maximum likelihood approach to emission image reconstruction from projections, IEEE Trans. Nucl. Sci. 23 (4) (1976) 1428–1432.

[13] R.G. Wells, et al., Maximizing the detection and localization of Ga-67 tumors in thoracic SPECT MLEM (OSEM) reconstructions, IEEE Trans. Nucl. Sci. 46 (4) (1999) 1191–1198.

[14] K.S. Chuang, et al., A maximum likelihood expectation maximization algorithm with thresholding, Comput. Med. Imag. Graph. 29 (7) (2005) 571–578.

[15] S.C. Keh, L.J. Meei, W. Jay, C. Sharon, C.N. Yu, K.F. Ying, The thresholding MLEM algorithm, J. Med. Biol. Eng. 24 (2) (2004) 85–91.

[16] H. Wieczorek, The image quality of FBP and MLEM reconstruction, Phys. Med. Biol. 55 (11) (2010) 3161–3176.

[17] A. Iriarte, R. Maraelementi, S. Matij, C.O.S. Sorzano, R.M. Lewitt, System models for PET statistical iterative reconstruction: a review, Comput. Med. Imag. Graph. 48 (Mar. 2016) 30–48.

[18] V. Maxim, et al., Probabilistic models and numerical calculation of system matrix and sensitivity in list-mode MLEM 3D reconstruction of Compton camera images, Phys. Med. Biol. 61 (1) (2016) 243–264.

[19] G.K. Loudos, An efficient analytical calculation of probability matrix in 2D SPECT, Comput. Med. Imag. Graph. 32 (2) (2008) 83–94.

[20] A. Rahmim, et al., Analytic system matrix resolution modeling in PET: an application to Rb-82 cardiac imaging, Phys. Med. Biol. 53 (2008) 5947–5965.

[21] S. Moehrs, et al., Multi-ray-based system matrix generation for 3D PET reconstruction, Phys. Med. Biol. 53 (2008) 6925–6945.

[22] K. Li, et al., A new virtual ring-based system matrix generator for iterative image reconstruction in high resolution small volume PET systems, Phys. Med. Biol. 60 (17) (2015) 6949–6973.

[23] K. Saha, K.J. Straus, Y. Chen, S.J. Click, Iterative reconstruction using a Monte Carlo based system transfer matrix for dedicated breast positron emission tomography, J. Appl. Phys. 116 (8) (2014) 1–11.

[24] M. Rafecas, et al., Use of a Monte Carlo-based probability matrix for 3-D iterative reconstruction of MADPET-II data, IEEE Trans. Nucl. Sci. 51 (2004) 2597–2605.

[25] V.Y. Panin, F. Kehren, C. Michel, M. Casey, Fully 3-D PET reconstruction with system matrix derived from point source measurements, IEEE Trans. Med. Imaging 25 (7) (2006) 907–921.

[26] D. Borys, K. Szczuka, K. Gorczewski, System matrix computation for iterative reconstruction algorithms in SPECT based on direct measurement, Int. J. Appl. Math. Comput. Sci. 21 (1) (2011) 193–202.

[27] F. Brown, J. Sweezy, J. Bull, J.T. Goorlay, A. Sood, MCNP - A General Monte Carlo N-Particle Transport Code Version 5, Los Alamos National laboratory, 2009.

[28] V. Moslemi, M. Ashoor, Evaluation of tomographic image quality of extended and conventional parallel hole collimators using maximum likelihood expectation maximization algorithm by Monte Carlo simulations, Nucl. Med. Commun. 38 (10) (2017) 843–853.

[29] V. Moslemi, M. Ashoor, Design and performance evaluation of a new high energy parallel hole collimator for radioiodine imaging by gamma cameras: Monte Carlo simulation study, Ann. Nucl. Med. 31 (4) (2017) 324–334.

[30] E.N. Gimenez, E. Nacher, M. Gimenez, J.M. Benlloch, M. Rafecas, Comparison of different approaches based on Monte Carlo methods to calculate the system matrix for small animal PET, Nucl. Instrum. Methods 569 (2) (2006) 346–349.

[31] Z. Wu, J. Liu, Experimental research on rear collimator in γ-ray industrial CT, Appl. Radiat. Isot. 67 (7) (2009) 1216–1219.

[32] V. Lohrabian, A. Kamali- Asl, H. Arabi, F. Mamashi, H.R. Hemmati, H. Zaidi, Design and construction of a variable resolution cone-beam small animal mini-CT prototype for in vivo studies, Radiat. Phys. Chem. 162 (2019) 199–207.

[33] B.J. Min, Y. Choi, N.Y. Lee, K. Lee, Y.B. Ahn, J. Joung, Design consideration of a multipinhole collimator with septa for ultra high-resolution silicon drift detector modules, Nucl. Instrum. Methods A. 606 (3) (2009) 755–761.